Received: 3 September 2024 | Revised: 31 October 2024 | Accepted: 27 November 2024

DOI: 10.1002/dug2.70014

RESEARCH ARTICLE

DUSE WILEY

Damage modeling of CO_2 injection well interfaces under coupled thermal, hydraulic and mechanical behavior

Lee J. Hosking | **Xiangming Zhou**

Brunel University of London, London, UK

Correspondence
Lee J. Hosking, Brunel University of London, Kingston Lane, Uxbridge, Middlesex, UB8 3PH, UK.
Email: lee.hosking@brunel.ac.uk

Funding information
UK Carbon Capture and Storage Research Community, Grant/Award Number: Flexible Funding Call (2023#20)

Abstract

This paper presents an investigation of well integrity during low-temperature CO_2 injection using a model of thermo-poroelasticity with interface damage mechanics. The casing–cement and cement–formation interfaces are described using cohesive interface elements and a bilinear traction–separation law. Verification testing is performed to establish the correct implementation of the coupled thermal, hydraulic, and mechanical equations. Simulation scenarios are developed to determine well interface damage initiation and development for intact wells and wells with an initial defect in the form of a 45° debonded azimuth. Each intact and defective well was simulated for 30 days of CO_2 injection at selected temperatures. Under the conditions considered, tensile radial stress developed at both the casing–cement and cement–formation interfaces. Hoop stress in the cement sheath remained compressive after 30 days but with reduced magnitude at the lower injection temperature, indicating greater risk of tensile stress and radial cracking as the injection temperature was reduced. Damage occurred in two of four scenarios considered, namely, the intact and defective wells at an injection temperature of 10°C, and was limited to the casing–cement interface, with no damage to the cement–formation interface. Inclusion of the pre-existing defect led to earlier damage initiation, at 2.75 days compared to 4 days, and produced a microannulus with over double the peak aperture at 0.077 mm compared to 0.037 mm. These findings emphasize the importance of accounting for initial defects and damage evolution when investigating the integrity of CO_2 injection wells.

KEYWORDS

CCS, damage modeling, interface debonding, well integrity

Highlights

- A model of thermo-poroelasticity with interface damage mechanics is developed.
- CO_2 injection at 10°C caused failure of the casing–cement interface.
- Lower injection temperature increased the risk of cement radial cracking.
- A pre-existing well defect caused earlier damage.
- A pre-existing well defect caused larger peak micro-annulus aperture.
- Well defects should be accounted for when predicting CO_2 leakage risk.

1 | INTRODUCTION

Global CO_2 emissions from fossil fuel combustion reached an all-time high of (35.8 ± 0.3) Gt CO_2 in 2023, 38.4% of which came from the power sector, with a further 29.0% from industry (Liu et al., 2024). Large-scale CO_2 capture and storage (CCS) is now widely seen as imperative for climate change mitigation, with cumulative amounts in the range of 348–1218 Gt CO_2 likely to be needed by 2100 (IPCC, 2018). Geological storage of captured CO_2 in deep saline aquifers and depleted oil and gas reservoirs is a large-capacity, long-term solution for emissions mitigation. However, the ability of these reservoirs to confine CO_2 may be compromised by natural and human-made leakage pathways, with upward CO_2 migration posing a risk to environmental and human health, and offsetting the

[Correction added on 31 May, 2025, after the first online publication: "Figure 18" has been amended.]

intended climate change mitigation if leaked CO_2 reaches the atmosphere (Roy et al., 2018; Zhang & Bachu, 2011). Impacts may be associated with free phase or dissolved CO_2 and any co-injected impurities affecting potable groundwater resources or terrestrial and marine ecosystems (Roberts & Stalker, 2020). At most CO_2 storage sites, there will be new injection wells planned, drilled, and completed to best practices, and there may be decommissioned oil and gas wells repurposed for CO_2 injection or left as legacy wells. All such wells penetrate confining layers with an integrity defined by their ability to maintain zonal isolation of geological formations by preventing upward fluid migration (Crow et al., 2010). With single barrier failures of cement and tubulars having been found in around one-third of North Sea oil and gas wells (King & King, 2013), well integrity will remain a key consideration in CO_2 storage risk and monitoring. Furthermore, offshore wells, which are expected to dominate the CCS sector in north-west Europe, present greater challenges in well control (Ahmed & Salehi, 2021; Sule et al., 2019).

Failure of one or more well barriers may or may not compromise well integrity (Ahmed & Salehi, 2021; King & King, 2013). This makes it important to understand how defects develop under different lifecycle conditions, leading to improved understanding of the stage of barrier degradation where well integrity issues can be expected to develop, and the extent of any loss of integrity in terms of the CO_2 leakage rate. It follows that well integrity largely depends on pre-existing defects and damage evolution due to drilling and completion, postcompletion thermal, hydraulic and mechanical (THM) loading, chemical (C) degradation (Carroll et al., 2016), and the efficacy of measures taken for plugging and abandonment. Common defects include microannulus formation by debonding at the casing–cement or cement–formation interfaces, mud channels from poor-quality cement placement, connection damage, and cement sheath cracking and dissolution (Ahmed & Salehi, 2021; Viswanathan et al., 2008), as illustrated in Figure 1.

CO_2 injection induces significant thermal loading due to the CO_2–formation temperature difference, Joule–Thomson cooling, and thermal cycling from periodic injection due to shutdowns or batch CO_2 transport by ship. Cold thermal loading of offshore injection wells is expected whether CO_2 is transported by ship or pipeline. For example, CO_2 transported to Snøhvit, Norway, is directly injected after exposure to North Sea seabed temperatures of around 4°C (Vilarrasa & Rutqvist, 2017). More extreme thermal loading may be expected when CO_2 is transported by ship at temperatures below −50°C. Even if some amount of CO_2 heating is used, modeling by Vilarrasa et al. (2013) suggests that injection temperatures of −20 to 5°C are possible, leading to significant thermal disturbance.

Experiments on mock-up well sections have shown that pressure and thermal cycling can cause interface debonding and damage evolution of defects in the cement sheath (de Andrade et al., 2014; Goodwin & Crook, 1992; Kuanhai et al., 2020; Li et al., 2016). Zhang and Eckert (2020) categorized these studies by two approaches: (1) those where cement is cured in the annulus between two casings with pressure applied to the inner casing after hardening (Goodwin & Crook, 1992; Jackson & Murphey, 1993; Therond et al., 2017), also referred to as the casing–casing annulus approach, and (2) those where the casing and cement are surrounded by a rock ring under confinement in a pressure vessel (de Andrade et al., 2015; Taghipour et al., 2022) or without confining pressure (Torsæter et al., 2017). Casing–casing annulus studies have reported damage development as a microannulus or radial cracking after removal or reduction of the inner casing pressure. Pressure vessel setups enable both pressure and thermal cycling, with de Andrade et al. (2015) reporting significant debonding at the casing–cement and cement–formation interfaces after thermal cycling with temperature differences of 140°C. Kuanhai et al. (2020) reported that integrity is considerably more sensitive to thermal cycling than pressure cycling.

The relationship between barrier failure by microannulus development and well integrity was explored in pressure

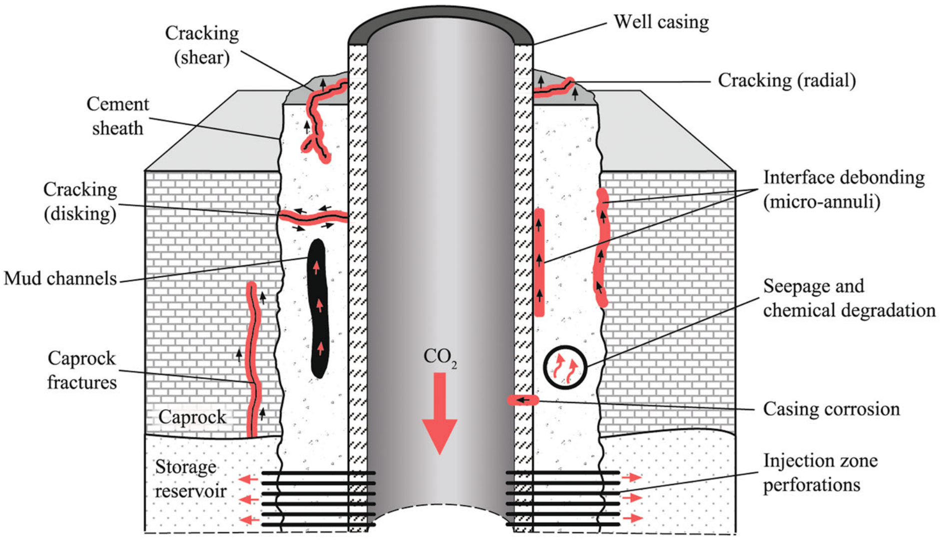

FIGURE 1 Common types of defects that may be encountered in CO_2 injection wells.

vessel experiments by Stormont et al. (2018). Various microannuli were generated using release film, thermal debonding, and corroded casing. They reported microannulus hydraulic apertures ranging from 10 to over 100 µm, corresponding to flow rates 10^3 to 10^5 times larger than intact specimens. Despite this, uncertainty remains over the practical leakage risk posed by microannuli: Duguid et al. (2018) presented cement bond logs (CBLs) for the CCS#1 injection well of the Decatur CCS project in the Illinois Basin, USA, identifying areas of casing–cement microannuli development from around 1700 m depth to the well bottom. This was attributed to minor cooling of around 5°C before CO_2 injection, while it is reported that the CO_2 injection pressure acted to close the microannuli in operation, since no major CO_2 leakage was observed during subsequent injection of 1 million tons of CO_2. Such practical observations show that damage development does not always lead to loss of integrity. However, the available field evidence is limited and experimental and computational modeling investigations of well damage under a broad range of conditions remain of value in pursuit of more informed leakage risk assessments for future projects.

Computational modeling studies have been pursued to characterize stress changes and failure modes in the composite casing–cement–formation well system (de Andrade & Sangesland, 2016; Lavrov, 2018; Liu et al., 2017; Roy et al., 2018). Figure 2 illustrates the interrelated disturbances to the thermal (T), hydrological (H), and mechanical (M) fields described by such models. Although chemical degradation via cement alteration and steel corrosion is another key aspect of the coupled behavior, it is beyond the scope of the present work and readers are referred to Carroll et al. (2016) in the first instance. Model representations of the in situ stress and displacement fields have been obtained by using "staged" numerical models that consider changes during drilling, casing, cementing, completion, pressure testing, and injection stages (Li et al., 2023; Zhang & Eckert, 2020). These studies handled the cement sheath as a poroelastoplastic material with interface bonds and microannulus development described using cohesive interface elements and a traction–separation law. A more common approach has been to express cement and interface failure modes using utilization factors defined as ratios of developed stresses to maximum allowable values taken as tensile and shear strengths (de Andrade & Sangesland, 2016; Lavrov, 2018; Roy et al., 2018; Valov et al., 2022). Onset of failure has been investigated for combinations of well loading (pressure and temperature), geometric defects such as casing stand-off, initial debonding, and thermo-mechanical properties of the cement and formation. Despite not considering cement sheath or interface damage evolution explicitly, the extensive failure criteria have provided important information about system dependencies. As examples, de Andrade and Sangesland (2016) identified a hierarchy of input parameters for performing sensitivity analyses, and Roy et al. (2018) presented failure risk zones for combinations of effective horizontal stress and injection temperature.

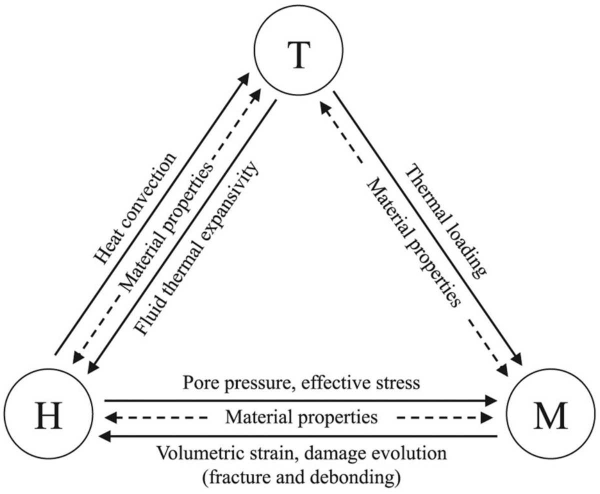

FIGURE 2 Schematic illustration of coupled thermal (T), hydraulic (H), and mechanical (M) processes relevant for modeling well integrity.

The present work uses numerical modeling of the CO_2 injection well system, with the cement sheath and formation handled as thermo-poroelastic materials and the casing–cement and cement–formation interfaces described using cohesive interface elements and a traction–separation law. Interface damage initiation and development are investigated under pressure and thermal loading, and for initially intact (perfectly bonded) and partially debonded interfaces. In this manner, the main contribution of this paper is to bridge the two types of studies mentioned above: (1) the staged numerical models, which have omitted initial defects due to the stringent and interdependent modeling stages involved, and (2) the utilization factor models, which cannot be used to predict the extent and aperture of debonding. The rest of this paper is organized as follows. Section 2 presents the basic equations of thermo-poroelasticity extended from the classical Biot theory, while Section 3 presents theory relating to the interface modeling. Section 4 describes the approach taken to extend the poroelastic storage model in COMSOL Multiphysics by coupling with the heat transfer module, as well as verification of the contact modeling problem for the interfaces. Sections 5, 6, and 7 are focused on defining the simulation scenarios and results presentation and discussion for the considered load cases and initial interface conditions. The conclusions are presented in Section 8.

2 | THEORETICAL MODEL FOR THERMO-POROELASTIC MEDIA

Considering the composite well system as a thermo-poroelastic body $\boldsymbol{\mathcal{B}} \subset \mathbb{R}^n (n = 2, 3)$ with external boundary $\partial\boldsymbol{\mathcal{B}} \subset \mathbb{R}^{n-1}$, the basic governing equations presented in this section are expressed in terms of spatial coordinates $\boldsymbol{x} \in \boldsymbol{\mathcal{B}}$ and time $t \in \mathcal{T} \subset \mathbb{R}_+$ as independent variables and displacements $\boldsymbol{u}$, pore fluid pressure p, and temperature T as dependent variables. The theory is established and applied in this study under the following assumptions:

1. The casing, cement sheath, and surrounding rock are linearly elastic, isotropic materials, with the casing being solid and the cement and rock being porous.
2. Pores in the cement and rock are fully saturated by a compressible and viscous fluid.

3. For the applications considered in this study, a plane strain approximation is adopted with deformation in the well axial direction considered small compared to deformation in the horizontal plane.
4. 2D well sections considered in this study lie above the injection zone such that the casing is not perforated and there is no mass transfer to/from the well tubing.
5. Strains are infinitesimal and the system is assumed to be quasi-static, allowing the reference and deformed configurations to be considered the same, with the Piola–Kirchhoff stress tensor S_{ij} being equivalent to the Cauchy stress tensor σ_{ij}.
6. The major and minor horizontal in situ stresses are aligned with the x and y axes, respectively.
7. The initial state of stress within the composite well system is assumed to be at equilibrium with the major and minor horizontal in situ stresses. Cement curing is assumed not to have altered the state of stress of the cement unless a prestress is specifically stated.
8. Chemical degradation is not considered in the present work.
9. Following the convention of COMSOL, stress and strain are positive in tension, while fluid pressure is positive in compression.
10. For the low rate of fluid flow envisaged, there is a state of local thermal equilibrium between the solid and pore fluid, such that $T_{\mathrm{f}} = T_{\mathrm{s}} = T$, where the subscripts f and s denote the pore fluid and solid phases, respectively.

The limitations associated with these assumptions should be acknowledged when considering practical application of the research findings presented in this study, especially for conditions that vary significantly from those considered.

2.1 | Deformation

For a quasi-static body, the mechanical equilibrium equation with respect to the reference configuration (and here also the deformed configuration) is

$$\frac{\partial \sigma_{ij}}{\partial x_j} + F_i = 0, \tag{1}$$

where σ_{ij} is the component of the Cauchy stress tensor and F_i is the component of the volumetric body force vector.

Under the aforementioned sign convention, the Cauchy stress tensor is expressed as

$$\sigma_{ij} = \sigma'_{ij} - \alpha_{\mathrm{B}} p \delta_{ij}, \tag{2}$$

where σ'_{ij} is the component of Biot's effective stress tensor, α_{B} is Biot's effective stress coefficient, and δ_{ij} is Kronecker's delta ($\delta_{ij} = 1$ for $i = j$, else $\delta_{ij} = 0$). α_{B} describes the change in pore fluid volume induced by a change in bulk volume in the drained condition, given by

$$\alpha_{\mathrm{B}} = 1 - \frac{K_{\mathrm{D}}}{K_{\mathrm{s}}}, \tag{3}$$

where K_{D} is the bulk modulus of the drained solid skeleton and K_{s} is the bulk modulus of the solid phase.

The effective stress σ'_{ij} represents the average stress in the solid skeleton and is given by the stress–strain constitutive relation:

$$\sigma'_{ij} = C_{ijkl} : \varepsilon_{kl}, \tag{4}$$

where C_{ijkl} is the component of the elastic stiffness matrix, ε_{kl} is the component of the total strain tensor, and the operator ':' denotes the double dot product expressed in general as $\boldsymbol{x} : \boldsymbol{y} = x_{ij}\, y_{ij}$.

Applying the Duhamel–Neumann extension of Hooke's law for a linearly thermoelastic isotropic material, Equation (4) becomes (Khalili & Selvadurai, 2003; Selvadurai & Nguyen, 1995)

$$\sigma'_{ij} = 2G\varepsilon_{ij} + \lambda \varepsilon_{kk}\delta_{ij} - \beta_{\mathrm{s}} K_{\mathrm{D}} T \delta_{ij}, \tag{5}$$

where G is the shear modulus, λ is Láme's constant, $\varepsilon_{kk} = \mathbf{tr}(\varepsilon_{ij})$ is the volumetric strain ε_{v}, and β_{s} is the coefficient of volumetric thermal expansion of the drained solid skeleton, noting that $\beta_{\mathrm{s}} = 3\alpha_{\mathrm{s}}$, with α_{s} being the coefficient of linear thermal expansion.

Substitution of Equation (5) into Equations (2) and (1) yields

$$\frac{\partial}{\partial x_j}(2G\varepsilon_{ij} + \lambda \varepsilon_{kk}\delta_{ij} - \alpha_{\mathrm{B}} p \delta_{ij} - \beta_{\mathrm{s}} K_{\mathrm{D}} T \delta_{ij}) + F_i = 0, \tag{6}$$

Finally, the strain–displacement relationship allows the strains ε_{ij} to be expressed in terms of the displacements $\boldsymbol{u}$ as the primary dependent variables:

$$\varepsilon_{ij} = \frac{1}{2}\left(\frac{\partial u_i}{\partial x_j} + \frac{\partial u_j}{\partial x_i}\right), \tag{7}$$

where u_i is the component of the displacement vector $\boldsymbol{u} = (u_x, u_y, u_z)$.

Substitution of Equation (7) into Equation (6) produces the set of partial differential equations governing the deformation behavior of the thermo-poroelastic medium:

$$\frac{\partial}{\partial x_j}\left[G\left(\frac{\partial u_i}{\partial x_j} + \frac{\partial u_j}{\partial x_i}\right) + \lambda \frac{\partial u_{\mathrm{k}}}{\partial x_{\mathrm{k}}}\delta_{ij} - \alpha_{\mathrm{B}} p \delta_{ij} - \beta_{\mathrm{s}} K_{\mathrm{D}} T \delta_{ij}\right] + F_i = 0. \tag{8}$$

2.2 | Fluid flow

From classical Biot poroelasticity theory, the mass conservation equation for the fluid-saturated porous medium is given by

$$\frac{\partial}{\partial t}(\rho_{\mathrm{f}}\phi) + \nabla\cdot(\rho_{\mathrm{f}}\boldsymbol{v}) = S_{\mathrm{m}}, \tag{9}$$

where ρ_{f} is the pore fluid's mass density, ϕ is the porosity, $\boldsymbol{v}$ is the velocity vector, and S_{m} is the fluid source/sink.

The first term on the left-hand side of Equation (9) is expanded as

$$\frac{\partial}{\partial t}(\rho_{\mathrm{f}}\phi)=\rho_{\mathrm{f}}\frac{\partial \phi}{\partial t}+\phi\frac{\partial \rho_{\mathrm{f}}}{\partial t}. \tag{10}$$

Following the approach of Selvadurai and Nguyen (1995), which is applied from Bishop (1973), the temporal derivatives of ϕ and ρ_{f} in Equation (10) may be obtained by examining the variations in ρ_{f} with dp and dT, and the variations in volume characteristics of an elemental volume V with dσ_{ij}, comprising dσ'_{ij} and dp, and dT. Use of this approach ultimately leads to the following expanded form of Equation (10) (Najari & Selvadurai, 2014; Selvadurai & Nguyen, 1995; Valov et al., 2022):

$$\begin{aligned}\frac{\partial}{\partial t}(\rho_{\mathrm{f}}\phi)=\rho_{\mathrm{f}}\Bigg[&\left(\frac{\phi}{K_{\mathrm{f}}}+\frac{\alpha_B-\phi}{K_{\mathrm{s}}}\right)\frac{\partial p}{\partial t}+\alpha_{\mathrm{B}}\frac{\partial \varepsilon_{\mathrm{v}}}{\partial t}\\&-(\phi\beta_{\mathrm{f}}+(\alpha_B-\phi)\beta_{\mathrm{s}})\frac{\partial T}{\partial t}\Bigg],\end{aligned} \tag{11}$$

where K_{f} is the bulk modulus of the pore fluid, related to the fluid compressibility χ_{f} by $K_{\mathrm{f}}=1/\chi_{\mathrm{f}}$, and β_{s} and β_{f} are the coefficients of volumetric thermal expansion of the solids and pore fluid, respectively.

With regard to the right-hand side of Equation (9), Darcy's law is used to describe fluid migration in the porous medium, yielding

$$\boldsymbol{v}=-\frac{k}{\mu}\nabla p, \tag{12}$$

where k is the permeability, recalling that the medium is assumed to be isotropic, and μ is the dynamic viscosity of the pore fluid. Owing to the plane strain case considered in this study, in which the 2D plane is horizontal, gravity effects are not included in Equation (12) (nor in Equation [9]).

Assuming that $\nabla\cdot(\rho_{\mathrm{f}}\boldsymbol{v})\approx\rho_{\mathrm{f}}\nabla\cdot\boldsymbol{v}$ after Selvadurai and Nguyen (1995), substitution of Equations (11) and (12) into Equation (9) with S_{m} as zero yields

$$\begin{aligned}&\left(\frac{\phi}{K_{\mathrm{f}}}+\frac{\alpha_{\mathrm{B}}-\phi}{K_{\mathrm{s}}}\right)\frac{\partial p}{\partial t}+\alpha_{\mathrm{B}}\frac{\partial \varepsilon_{\mathrm{v}}}{\partial t}-(\phi\beta_{\mathrm{f}}+(\alpha_{\mathrm{B}}-\phi)\beta_{\mathrm{s}})\\&\frac{\partial T}{\partial t}=\frac{k}{\mu}\nabla^2 p,\end{aligned} \tag{13}$$

where $\nabla^2=\nabla\cdot\nabla$ is the Laplacian.

Equation (13) without the thermal terms is the governing equation for poroelasticity implemented as standard in COMSOL, extended here based on established theory to account for thermal effects under the framework of thermo-poroelasticity.

2.3 | Heat transfer

The energy conservation equation for heat transfer in porous media is given by

$$\frac{\partial}{\partial t}((\rho C)_{\mathrm{avg}}T)+\nabla\cdot\boldsymbol{Q}+\rho_{\mathrm{f}}C_{\mathrm{f}}\boldsymbol{v}\nabla T=S_{\mathrm{h}}, \tag{14}$$

where ρ is the bulk density, $\boldsymbol{Q}$ is the conductive heat flux vector, C_{f} is part of the term concerning heat convection and represents the gravimetric specific heat capacity of the pore fluid, S_{h} is the source/sink, and the term $(\rho C)_{\mathrm{avg}}$ is the average specific heat capacity of the saturated porous medium, defined as

$$(\rho C)_{\mathrm{avg}}=\phi\rho_{\mathrm{f}}C_{\mathrm{f}}+(1-\phi)\rho_{\mathrm{s}}C_{\mathrm{s}}, \tag{15}$$

where C_{s} and ρ_{s} are the specific heat capacity and density of the solid phase, respectively.

The conductive heat flux vector $\boldsymbol{Q}$ is defined as

$$\boldsymbol{Q}=-\lambda_{\mathrm{avg}}\nabla T, \tag{16}$$

where λ_{avg} is the average thermal conductivity of the saturated porous medium, given by

$$\lambda_{\mathrm{avg}}=\phi\lambda_{\mathrm{f}}+(1-\phi)\lambda_{\mathrm{s}}, \tag{17}$$

where λ_{f} and λ_{s} are the thermal conductivities of the pore fluid and solid phases, respectively.

Since the rate of convective heat transfer is proportional to the fluid flow rate, its significance in low-permeability porous media, such as many rocks, can often be considered negligible. Adopting this simplification and substituting Equations (15)–(17) into Equation (14) with $S_{\mathrm{h}}=0$ yield the governing equation for heat transfer

$$(\phi\rho_{\mathrm{f}}C_{\mathrm{f}}+(1-\phi)\rho_{\mathrm{s}}C_{\mathrm{s}})\frac{\partial T}{\partial t}=-\lambda_{\mathrm{avg}}\nabla^2 T, \tag{18}$$

Together, Equations (8), (13), and (18) represent the governing equations describing thermo-poroelastic behavior under the stated assumptions. While many of the terms of these equations are implemented in COMSOL's *Solid Mechanics*, *Darcy's Law*, and *Heat Transfer in Porous Media* interfaces, only the poroelastic coupling terms are accounted for. The additional terms relating to the thermal couplings have been added.

3 | INTERFACE MODEL

Bonding strength between the cement sheath and the casing and formation develops during cement hardening (Zhang et al., 2017). In this study, the interfaces at the casing–cement and cement–formation internal boundaries $\partial\mathcal{B}_i\subset\mathbb{R}^{n-1}$ are modeled as contact surfaces with cohesive behavior using interface elements. Microannulus initiation and growth are effectively handled as a process of progressive fracture (i.e., decohesion) at these boundaries, implemented using a mixed-mode bilinear traction–separation law. Figure 3 is a generalized representation of the relationship between traction and separation for a single mode of failure, which may be crack opening in the normal direction (mode I, subscript

n) or due to shear (modes II/III, subscripts s, t). Various stages of microannulus initiation and development are illustrated, comprising linear–elastic pre-damage behavior (OA), damage evolution behavior (AC), and irrecoverable damage with unloading (BO). A scalar damage variable d describes the extent of interface damage ranging from fully intact ($d = 0$) to fully damaged ($d = 1$) based on both the normal and tangential components of an adhesive stress vector $\boldsymbol{f}$:

$$\boldsymbol{f} = (1 - d)\boldsymbol{K\delta}, \tag{19}$$

where $\boldsymbol{K}$ is the adhesive stiffness vector with the two tangential components of stiffness assumed to be equal in this study and $\boldsymbol{\delta}$ is the displacement jump vector. Considering normal and shear failure modes, a mixed-mode displacement δ_{m} is defined as the norm of $\boldsymbol{\delta}$, yielding $\delta_{\mathrm{m}} = \lVert\boldsymbol{\delta}\rVert$. The initiation of damage is then defined using the mixed-mode criterion (COMSOL, 2022):

$$\delta_{\mathrm{m}0} = \delta_{\mathrm{n}0}\delta_{\mathrm{s}0}\left(\frac{\delta_{\mathrm{m}}^2}{\langle\delta_{\mathrm{I}}\rangle^2\delta_{\mathrm{s}0}^2 + \delta_{\mathrm{II}}^2\delta_{\mathrm{n}0}^2}\right)^2, \tag{20}$$

where $\delta_{\mathrm{m}0}$ is the mixed-mode displacement at initiation of damage, δ_{I} and δ_{II} are the mode I and II displacements, respectively, with $\langle\delta_{\mathrm{I}}\rangle = \delta_{\mathrm{I}}$ if $\delta_{\mathrm{I}} \geq 0$ else $\langle\delta_{\mathrm{I}}\rangle = 0$ to account for any overclosure in interface compression, and $\delta_{\mathrm{n}0}$ and $\delta_{\mathrm{s}0}$ are displacement constants based on the following ratios:

$$\delta_{\mathrm{n}0} = \frac{\sigma_{\mathrm{n}0}}{K_{\mathrm{n}}}, \tag{21}$$

$$\delta_{\mathrm{s}0} = \frac{\sigma_{\mathrm{s}0}}{K_{\mathrm{s}}}, \tag{22}$$

where $\sigma_{\mathrm{n}0}$ and $\sigma_{\mathrm{s}0}$ are the normal (tensile) and shear strengths of the adhesive layer, respectively, and K_{n} and K_{s} are the normal and tangential stiffness components of $\boldsymbol{K}$, respectively. Since damage is irrecoverable, stiffness after damage adopts the secant modulus, reducing by a factor of $(1 - d)$, as illustrated by path BO in Figure 3.

At the point of damage initiation, $\delta_{\mathrm{m}} = \delta_{\mathrm{m}0}$ and Equation (20) can be rearranged to a quadratic interaction function defining failure at point A in terms of normal and shear displacement ratios:

$$\left(\frac{\langle\delta_{\mathrm{I}}\rangle}{\delta_{\mathrm{n}0}}\right)^2 + \left(\frac{\delta_{\mathrm{II}}}{\delta_{\mathrm{s}0}}\right)^2 = 1. \tag{23}$$

Damage evolution along path AC in Figure 3 is based on the Benzeggagh–Kenane fracture energy criterion (Benzeggagh & Kenane, 1996):

$$G_{\mathrm{cn}} + (G_{\mathrm{cs}} - G_{\mathrm{cn}})\left(\frac{G_{\mathrm{II}}}{G_{\mathrm{I}} + G_{\mathrm{II}}}\right)^{\alpha} = G_{\mathrm{cT}}, \tag{24}$$

where G_{cn}, G_{cs}, and G_{cT} are the normal (tensile), shear, and total strain energy release rates, respectively, α is the mixed-mode exponent, and G_{I} and G_{II} are the mode I and II strain energies, respectively. Equation (24) allows the mixed-mode failure displacement δ_{mf} to be determined, which defines the damage evolution (i.e., path AC in Figure 3).

4 | MODEL IMPLEMENTATION AND VERIFICATION

As mentioned earlier, three COMSOL physics interfaces are used to develop the previous governing equations. They are the *Solid Mechanics*, *Darcy's Law*, and *Heat Transfer in*

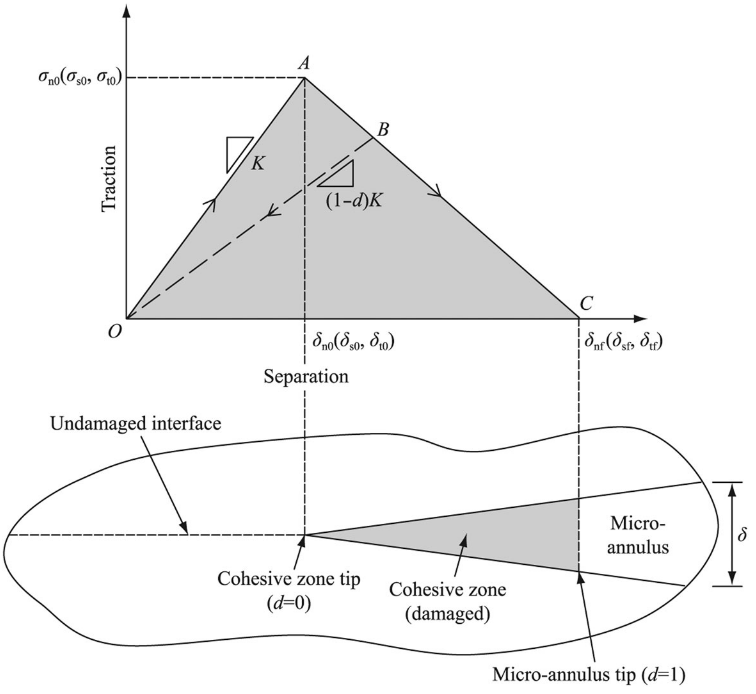

FIGURE 3 A generalized bilinear traction–separation law illustrating the relationship between traction and separation for a single mode of failure. This study uses a mixed-mode law based on the combined actions of modes I and II. The schematic in the lower panel illustrates how the traction–separation law relates to different stages of microannulus initiation and development.

Porous Media interfaces. Coupling for poroelasticity (HM) is readily available in COMSOL, but additional terms have been added for thermal expansion in Equation (8) and the fluid mass source/sink in Equation (13). The casing–cement and cement–formation interface model described is handled as a contact model with decohesion in the *Solid Mechanics* interface.

Verification of the coupled model is pursued using a one-dimensional (1D) thermo-poroelastic problem described by Selvadurai and Suvorov (2016). The problem considers a porous column of finite height with 1D deformation achieved by applying uniform stress, fluid pressure, and temperature change to the upper surface, while the displacement, fluid velocity, and heat flux normal to other surfaces are set to zero, as shown in Figure 4. Since derivation of the set of analytical solutions for temperature, pore pressure, and displacement can be found in Selvadurai and Suvorov (2016), here, the initial and boundary conditions and associated solutions are presented in summary form in Appendix A.

Table 1 presents the variables and parameters used as input for the analytical benchmarks. For ease of comparison, these inputs are duplicated from Selvadurai and Suvorov (2016). Since COMSOL requires distinct properties for the solid and fluid phases, these have been determined from the ratios λ^*/C^* and k/μ by assuming water as the pore fluid, allowing the solid-phase properties and permeability to be determined, as shown in Table 2.

TABLE 1 Variables and parameters describing the thermo-poroelastic problem used to verify the coupled thermal, hydraulic and mechanical (THM) model, expressed in terms related to analytical solutions in Appendix A.

Variable or parameter	Value
Length, L (m)	10
Initial temperature step, T_0 (°C)	50
Biot coefficient, α_B	0.75
Porosity, ϕ	0.25
Drained bulk modulus, K_D (GPa)	5
Solid bulk modulus, K_s (GPa)	20
Pore fluid bulk modulus, K_f (GPa)	2.2
$K_D + 4G_D/3$ (GPa)	8.1
Solid thermal expansion coefficient, α_s (10^{-6} °C^{-1})	8.3
Fluid thermal expansion coefficient, α_f (10^{-5} °C^{-1})	6.9
λ^*/C^* (10^{-6} m^2/s)	1.6
k/μ (10^{-16} m^3·s/kg)	6.0

TABLE 2 Additional parameters derived from Table 1 to define the thermo-poroelastic model in COMSOL.

Variable or parameter	Value
Solid density, ρ_s (kg/m^3)	1600
Fluid density, ρ_f (kg/m^3)	1000
Solid gravimetric specific heat capacity, C_s (J·kg^{-1}·K^{-1})	800
Solid gravimetric specific heat capacity, C_f (J·kg^{-1}·K^{-1})	4180
Solid thermal conductivity, λ_s (W·m^{-1}·K^{-1})	4.5
Fluid thermal conductivity, λ_f (W·m^{-1}·K^{-1})	0.65
Permeability, k (10^{-19} m^2)	6.0
Fluid viscosity, μ (10^{-3} Pa·s)	1.0

Note: Parameters derived from the overall properties (k_c^*, c_p^*) and viscosity have assumed water to be the pore fluid. Other input values represent an unspecified geomaterial satisfying the ratios in Table 1.

The adopted test case considers the 1D thermo-poroelastic response of the column for $\sigma_0 = 0$, $\overline{T}_0 = 0$°C, and $T_0 = 50$°C. This means that the temperature of the column is uniformly increased from 0 to 50°C at $t = 0$ in the form of a Heaviside step function $H(t)$. While this step is arbitrary, it serves a computational purpose by disturbing the temperature field to examine the coupled response of displacement and pore pressure. The subsequent evolution of the system is driven by the constrained temperature and drained boundary conditions at the upper surface. It should be noted that no pore water phase transformations are considered.

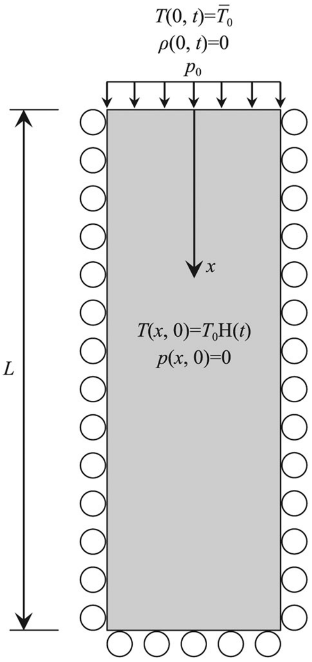

FIGURE 4 Schematic of the two-dimensional domain used to simulate the one-dimensional problem of thermo-poroelasticity considered by Selvadurai and Suvorov (2016). $H(t)$ is the Heaviside step function used to denote a uniform increase in temperature from $\overline{T}_0$ to T_0 across the domain at $t = 0$.

Figure 5 presents the temperature distribution in the column along x at selected times with agreement between the analytical solutions, shown as points, and the numerical solutions, shown as solid lines. The temperature gradually reduces from 50 to 0°C, as expected. Small differences between the solutions as time increases are attributed to the assumptions made in deriving the fluid- and solid-phase properties, as explained above. Distributions of pore pressure at the same output times are presented in Figure 6, once more with agreement between the analytical and numerical solutions. The step change in temperature resulted in a large increase in pore pressure, increasing from 0 to over 12 MPa due to the thermal

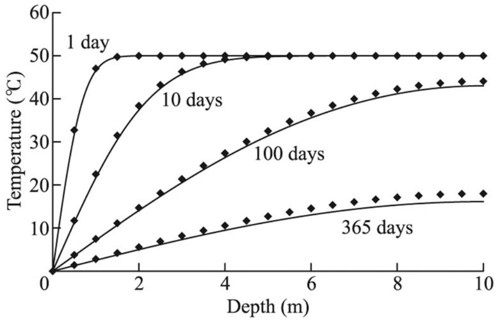

FIGURE 5 Temperature distribution along x at selected times following the 50°C step and subsequent heat flow to the upper boundary. Analytical solutions are shown as points and numerical solutions are shown as solid lines.

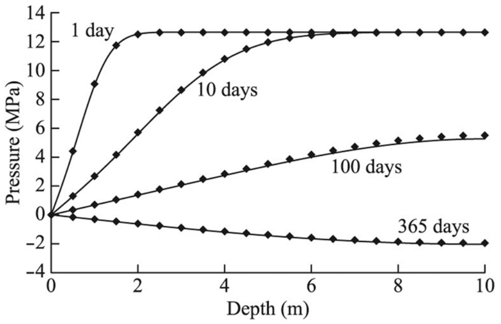

FIGURE 6 Pore pressure distribution along x at selected times following the 50°C step and the imposition of a drained condition at the upper boundary. Analytical solutions are shown as points and numerical solutions are shown as solid lines.

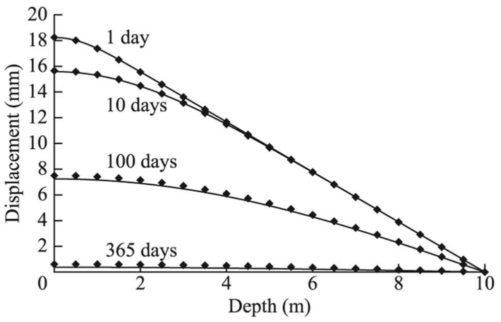

FIGURE 7 Vertical displacement distribution along x at selected times following the 50°C step and subsequent heat and mass transfer to the upper boundary. Positive displacement represents expansion of the column. Analytical solutions are shown as points and numerical solutions are shown as solid lines.

mass source term in Equation (13). This behavior results from the system being undrained for the initial temperature step at $t = 0$. Once drained conditions are established for $t > 0$, the pore pressure decreases and eventually becomes negative as the temperature continues to decline. Figure 7 presents the vertical displacement along x, reflecting the initial thermal expansion of the column, followed by a return toward zero displacement.

Comparisons between the analytical and numerical solutions for coupled THM behavior in this section have served to verify the thermo-poroelastic model. Additional verification for the interface model is not necessary, since this study is using in-built features of the *Solid Mechanics* interface in COMSOL. The only difference is that changes in stress at the interface are now based on the coupled THM behavior considered above rather than the pre-existing HM behavior.

5 | WELLBORE MODEL AND SIMULATION SCENARIOS

Four simulation scenarios are defined to study the influence of CO_2 injection temperature and initial defects on well integrity. As summarized in Table 3, the first set of two simulations considers initially perfectly bonded casing–cement and cement–formation interfaces, while the second set of two simulations introduces a debonded surface representing a defect from the cement job. Apart from the initial defect, the simulation domain remains the same in terms of geometric and material properties, as reported in Tables 4 and 5. As shown in Figure 8, the 2 m by 2 m domain comprises one quarter of a 2D plane strain well section located above the injection zone in the cap rock. Since the section is taken in the cap rock, there is no mass transfer to/from the tubing. The debonded surface is taken here as a 45° azimuth of the quarter plane considered. The cement and rock are assumed to be fully saturated by water and the system has an initial temperature of 323 K and a pore pressure of 15 MPa, representing conditions at a depth of around 1.5 km. According to assumption 7

TABLE 3 Summary of the simulation test cases considered in this study.

Test case	T_{in} (°C)	p_{in} (MPa)	Initial defect? (Y/N)
A1	20	20	N
A2	10	20	N
B1	20	20	Y (casing–cement)
B2	10	20	Y (casing–cement)

Note: T_{in} and p_{in} are the injection temperature and pressure, respectively, applied using ramp functions during the first 1 day of the simulation. Defects are identified by the azimuthal extent and the location of initial debonding.

TABLE 4 Geometric and material parameters used for the test cases considered in this study.

Parameter	Casing	Cement	Formation
Porosity (−)	–	0.2	0.2
Permeability (mD)	–	0.001	0.1
Biot coefficient (−)	–	0.6	0.6
Thermal conductivity ($W \cdot m^{-1} \cdot K^{-1}$)	50	1	2.1
Coeff. thermal expansion ($10^{-5} K^{-1}$)	1.2	1.0	0.8
Specific heat capacity ($J \cdot kg^{-1} \cdot K^{-1}$)	450	1600	1000
Density (kg/m^3)	8000	2240	2240
Young's modulus (GPa)	200	10	50
Poisson's ratio (−)	0.3	0.25	0.3

in Section 2, the initial state of stress within the composite well system is assumed to be at equilibrium with the major and minor horizontal in situ stresses, which, here, have an equal magnitude of 25 MPa. The outer boundaries have the temperature and pore pressure constrained at the initial values to represent the far field.

A simulation period of 30 days is considered, with the thermo-mechanical disturbance caused by CO_2 injection being represented by boundary conditions imposed on the inner surface of the casing. To better reflect realistic well operation and provide numerical stability, these conditions are implemented using ramp functions as

$$T(t) = T_{\text{in}} R(t), \tag{25}$$

$$p(t) = p_{\text{in}} R(t), \tag{26}$$

where T_{in} and p_{in} are the final injection temperature and pressure, respectively, shown in Table 3, and $R(t)$ is a ramp function defined as

$$R(t) = \begin{cases} 0 & \text{if } t = 0, \\ 1 & \text{if } t \geq 1 \text{ day}. \end{cases} \tag{27}$$

TABLE 5 Interface parameters used for the test cases considered in this study.

Parameter	Casing
Normal strength (MPa)	0.5
Shear strength (MPa)	2.0
Adhesive normal stiffness (GPa/m)	$60/h_{\text{min}}$
Adhesive shear stiffness (GPa/m)	$\frac{K_n(1-2\nu)}{2(1-\nu)}$
Energy release rate (J/m^2)	100
BK exponent (−)	2.0

Note: The same values are assumed for both the casing–cement and cement–formation interfaces, based on Zhang and Eckert (2020). h_{min} is the minimum element size on the destination boundary defined by the contact pair in COMSOL.

6 | SIMULATIONS OF INTACT WELLS

Results for intact test cases A1 (T_{in} = 20°C) and A2 (T_{in} = 10°C) are presented in this section, representing wells with initially perfectly bonded casing–cement and cement–formation interfaces. Figures 9 and 10 show the

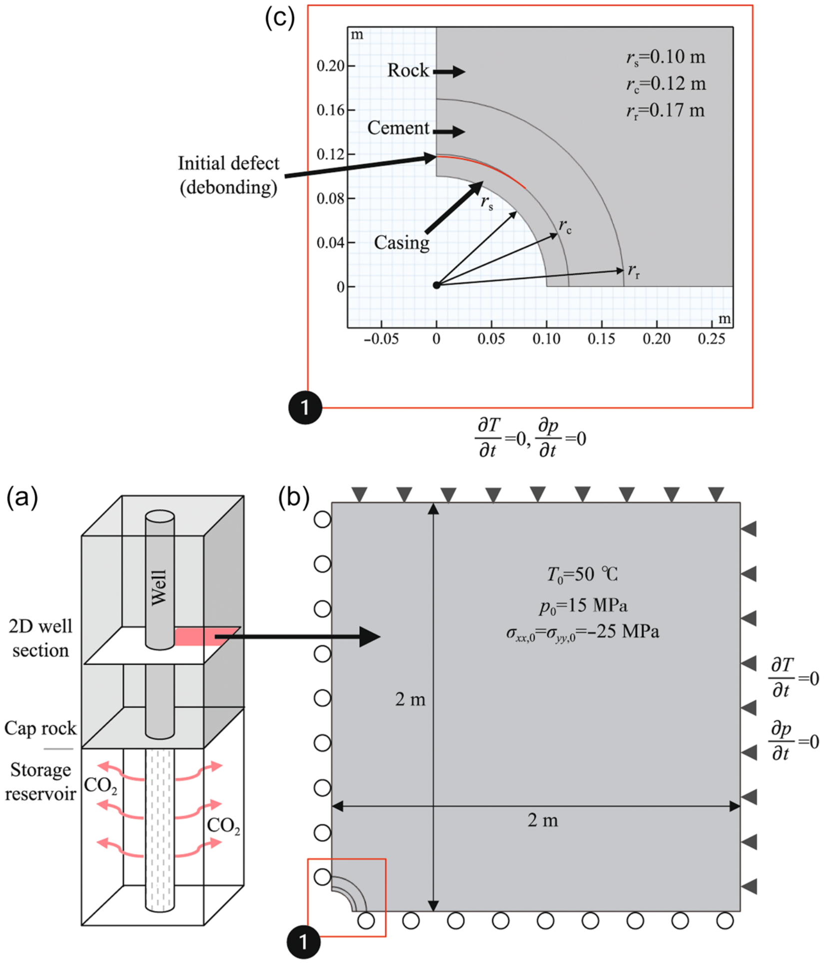

FIGURE 8 Summary of the simulation domain: (a) location of a 2D plane in the cap rock with one quarter of the plane used as the simulation domain and (b, c) geometry and initial/boundary conditions (pressure and temperature conditions applied to the inner surface of the casing are explained separately).

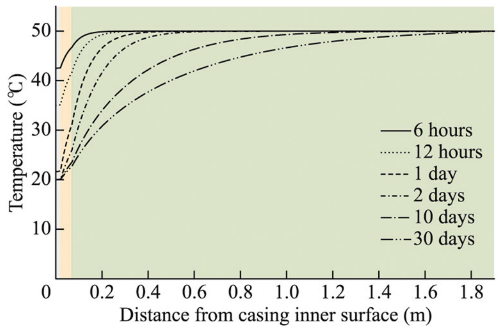

FIGURE 9 Distribution of temperature with distance from the inner casing surface for test A1 ($T_{\text{in}} = 20°\text{C}$), taken along the lower boundary of the domain. Shading is used to indicate the casing, cement, and rock formation.

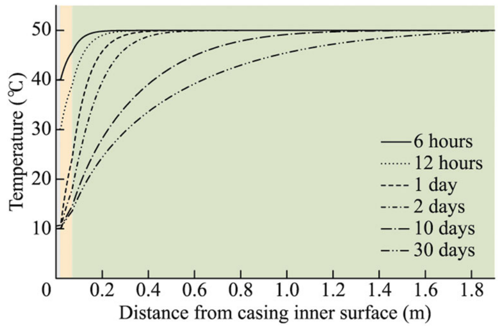

FIGURE 10 Distribution of temperature with distance from the inner casing surface for test A2 ($T_{\text{in}} = 10°\text{C}$), taken along the lower boundary of the domain. Shading is used to indicate the casing, cement, and rock formation.

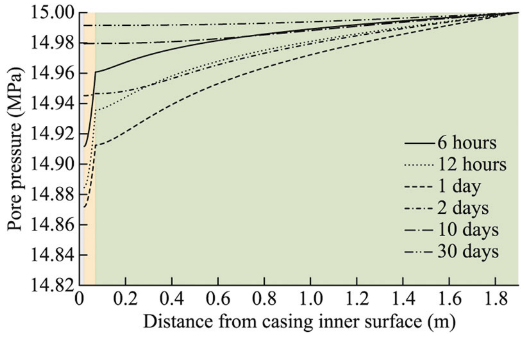

FIGURE 11 Distribution of pore pressure with distance from the inner casing surface for test A1 ($T_{\text{in}} = 20°\text{C}$), taken along the lower boundary. Shading indicates the casing, cement, and rock formation.

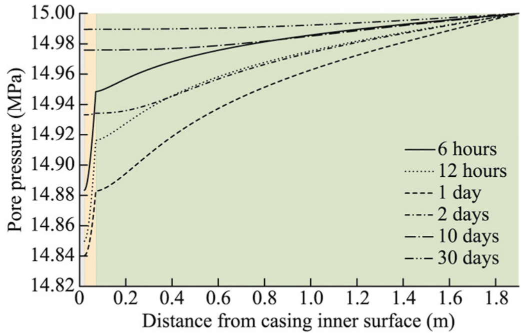

FIGURE 12 Distribution of pore pressure with distance from the inner casing surface for test A2 ($T_{\text{in}} = 10°\text{C}$), taken along the lower boundary of the domain. Shading is used to indicate the casing, cement, and rock formation.

evolution of temperature with distance from the casing inner surface, which was one of the main drivers of change alongside injection pressure. The results follow the expected trend considering the imposed reduction in injection temperature from T_0 to T_{in} during the first day of the simulation period. As expected, considering its significantly higher thermal conductivity and lower specific heat capacity, the casing temperature always changed rapidly and remained nearly uniform across its thickness. By comparison, the evolution of cement and formation temperature was more gradual and did not reach equilibrium during the 30-day simulation period.

Disturbances in pore pressure at selected times in tests A1 and A2 are shown in Figures 11 and 12, respectively. No significant changes were observed mainly because the domain section is situated in the cap rock above the injection interval. This means that the small changes in pore pressure can be attributed to the second and third coupling terms on the left-hand side of Equation (13). The second (hydro-mechanical) coupling term describes the change in pore volume with bulk volume, while the third (thermo-hydraulic) term describes the changes in pore fluid and solid-phase volumes with temperature. Small decreases in pore pressure from the initial 15 MPa were observed in both tests in the cement and formation near the well, decreasing to 14.87 MPa in test A1 and 14.85 MPa in test A2 after 1 day of simulation, during which time the well pressure and temperature were increased using the ramp functions shown in Equations (25)–(27). Once the pressure and temperature in the injection well were stabilized for $t \geq 1$ day, the pore pressure returned toward 15 MPa as water flowed inward from the far field. The initial decline in pore pressure indicates the coupled THM response of a small increase in pore volume and a small fluid shrinkage. It is noted that the pore fluid is prescribed using the in-built water material model in COMSOL, which includes relationships for the evolution of properties, including density, viscosity, thermal conductivity, and specific heat capacity. While the observed changes in pore pressure were small under these simulation conditions, this is not expected to be the case when the present work is extended to consider the mass transfer of CO_2 from the injection well, giving rise to the displacement of in situ pore water in the near-well region under multiphase flow.

Figures 13 and 14 show the distribution of radial and tangential (hoop) stress with distance from the casing inner surface after the 30-day simulation period. Only the first 0.5 m is plotted to allow closer inspection of trends near the well, and vertical shading is used to indicate the casing, cement sheath, and formation. For the adopted sign convention, positive values denote tensile stress. It can be seen that tensile radial stress developed at the casing–cement and cement–formation interfaces in both tests, with the larger stress being at the casing–cement interface. Variations in hoop stress were more pronounced, with significant snap-through behavior (discontinuity) between the different

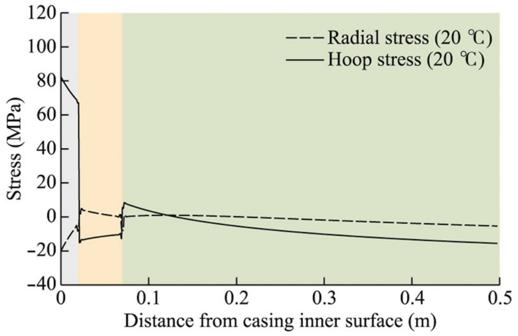

FIGURE 13 Distribution of radial and hoop stress with distance from the inner casing surface for test A1 (T_{in} = 20°C) after 30 days, taken along the lower boundary. Shading indicates the casing, cement, and rock formation.

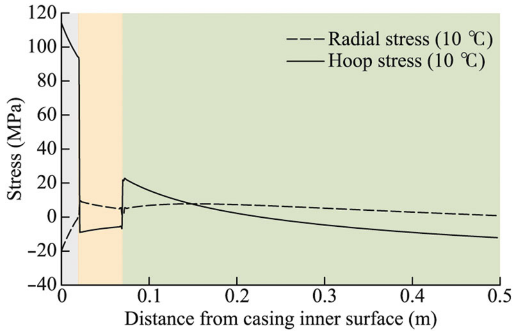

FIGURE 14 Distribution of radial and hoop stress with distance from the inner casing surface for test A2 (T_{in} = 10°C) after 30 days, taken along the lower boundary. Shading indicates the casing, cement, and rock formation.

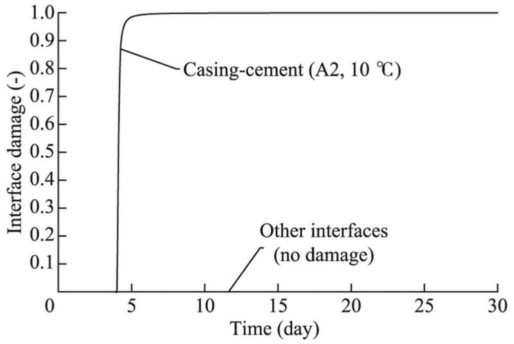

FIGURE 15 Evolution of interface damage for intact tests A1 (T_{in} = 20°C) and A2 (T_{in} = 10°C).

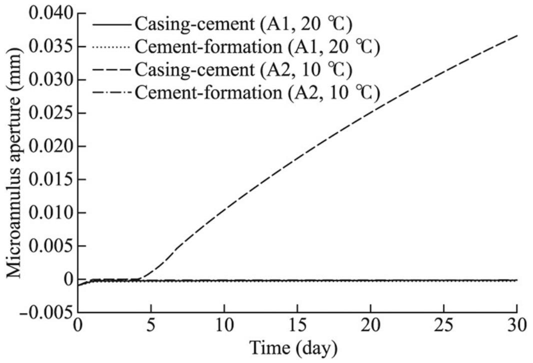

FIGURE 16 Evolution of the microannulus aperture for intact tests A1 (T_{in} = 20°C) and A2 (T_{in} = 10°C).

materials of the composite well system. This behavior is consistent with other studies on oil, gas, and geothermal wells (Huan et al., 2021; W. Liu et al., 2017). Tensile hoop stress was largest in the casing and notably larger for lower T_{in}. It is worth noting that hoop stress in the cement sheath was compressive at the end of both simulations, although the compressive stress became smaller (i.e., more toward tension) for lower T_{in}, reaching −5 MPa in test A2 compared to −10 MPa in test A1. This suggests that the development of tensile hoop stress in the cement sheath becomes more likely at lower injection temperatures, which may lead to radial cracking if the tensile strength is exceeded.

Having examined the coupled THM response of the well system, Figures 15 and 16 show the evolution of interface damage and microannulus aperture for tests A1 and A2, respectively. No damage ($d = 0$) to either the casing–cement or cement–formation interfaces was predicted in test A1 (T_{in} = 20°C), while in test A2 (T_{in} = 10°C), there was complete damage ($d = 1$) with microannulus growth at the casing–cement interface after 4 days, but no damage at the cement–formation interface. In the absence of defects and with $\sigma_{xx,0} = \sigma_{yy,0}$, the interface damage development and microannulus growth occurred in the same manner across the 90° azimuth considered. The microannulus aperture in test A2 increased consistently after initiation at 4 days, reaching 0.037 mm at the end of the 30-day simulation period. As was the case for damage evolution, the microannulus developed uniformly. It is worth noting that the small negative apertures at small times in Figure 16 reflect small overclosure associated with the penalty stiffness of the interface. While the overclosure can be reduced by prescribing higher stiffness, this must be balanced with reduced stability (COMSOL, 2022).

The steep curve in Figure 15 reflects a rapid failure of the interface following damage initiation, with $d = 0$ at 4 days and $d = 0.99$ at 5.4 days. This implies brittle failure of the interface with limited separation, although it is noted that further investigation is needed to determine the dependence of this behavior on the interface model parameters in Table 5. It is also worth noting that some authors have defined the same interface parameters at both the casing–cement and cement–formation interfaces (Zhang & Eckert, 2020), as was the case here, while others have specified a lower strength cement–formation interface (Li et al., 2023). The investigation of such uncertainties is beyond the scope of the present work and should be recognized as a limitation to be addressed in future work.

7 | SIMULATIONS OF DEFECTIVE WELLS

Results for test cases B1 (T_{in} = 20°C) and B2 (T_{in} = 10°C) for a well with an initial defect at the casing–cement interface are presented in this section. As explained in Section 5 and depicted in Figure 8, the debonded surface extends for an azimuth of 45° and is represented by surfaces in contact but lacking adhesion. Considering that all other conditions in tests B1 and B2 remain the same as in tests A1 and A2, the THM behavior follows similar trends and is not revisited for brevity. Instead, the focus is on determining the impact of the initial defect on damage initiation and development.

Figure 17 shows the damage to both interfaces in tests B1 and B2. Introduction of the defect did not lead to damage development at either interface at the higher injection temperature (test B1), perhaps indicating a greater dependence on thermal loading than the presence of pre-existing defects under the conditions studied. Damage initiation at the lower injection temperature (test B2) occurred earlier at 2.75 days compared to 4 days in test A2, and showed a significantly different trend due to the nonuniform condition of the casing–cement interface with the defect. This nonuniformity is illustrated by the different displacement contour plots after 30 days for tests A2 and B2 in Figure 18. While the overall trend of displacement was fairly consistent for the two simulations, there were clear differences in the microannulus shape, which became nonuniform with azimuth following introduction of the defect. Accordingly, Figure 17 includes two damage curves for test B2: one at an azimuth of 0° and the other at 45°. It can be seen that damage was initiated at the tip of the defect at 45° azimuth and only reached 0° azimuth toward the end of the simulation period. By comparison, the damage for intact test A2 was initiated later but was uniform with azimuth.

More information on the nonuniform casing–cement microannulus developed in test B2 is provided by plotting the evolution of aperture at azimuths of 0°, 45°, and 90° in Figure 19. The microannulus aperture for test A2 is also plotted as a reference and all displacements are increased by a factor of 100. It is clearly shown that the magnitude of the microannulus aperture increased with azimuth, with the largest aperture being 0.077 mm at 90° azimuth after 30 days. This is 2.08 times larger than the maximum aperture predicted for the intact test A2. Aperture growth at 45° azimuth followed a similar trend to that of test A2, increasing to 0.039 mm after 30 days. There was limited aperture growth at 0° azimuth due to the fact that damage was only initiated after 27 days. These findings indicate that the pre-existing debonded surface had a somewhat limited impact on damage initiation, which occurred only slightly earlier, but a larger impact on the peak microannulus

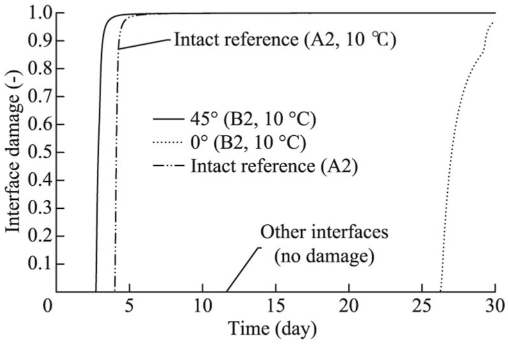

FIGURE 17 Evolution of casing–cement interface damage at two locations for defective tests B1 ($T_{\text{in}} = 20°\text{C}$) and B2 ($T_{\text{in}} = 10°\text{C}$). Locations are represented by azimuth from the x-axis and damage from test A2 is included as a reference.

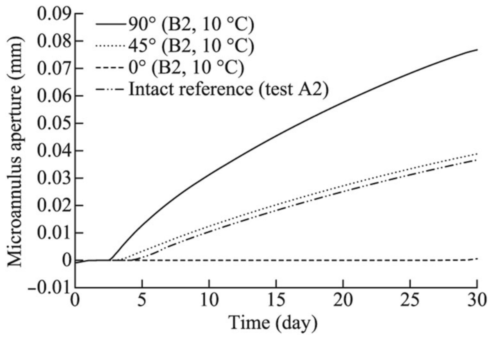

FIGURE 19 Evolution of the microannulus aperture at three locations for defective test B2 ($T_{\text{in}} = 10°\text{C}$). Locations are represented by azimuth from the x-axis and the aperture from test A2 is included as a reference.

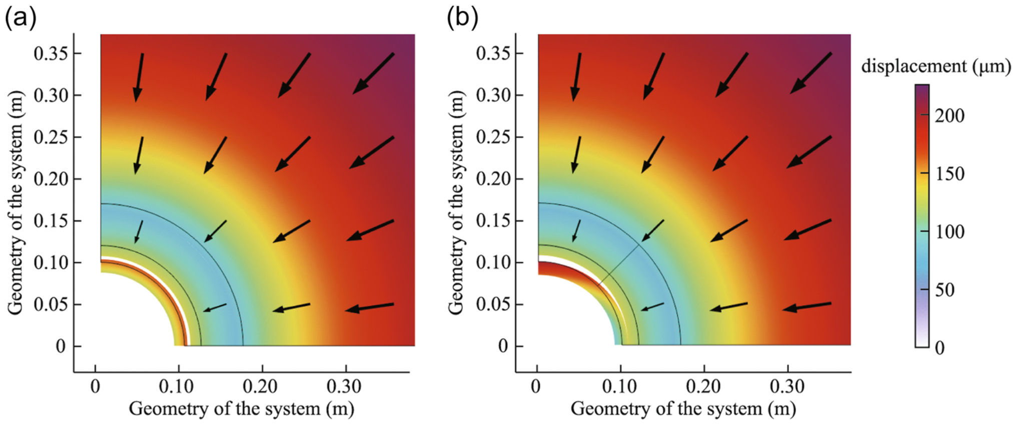

FIGURE 18 Contour plots of displacement magnitude at 30 days, with an arrow surface also used to show the direction and the relative magnitude of displacement for (a) intact test A2 and (b) defective test B2 (both for $T_{\text{in}} = 10°\text{C}$).

aperture. Lacking any resistance to opening, the presence of a defect produced a nonuniform microannulus with a significantly larger peak aperture. For the sake of simplicity, let us assume that vertical fluid flow in the microannulus can be treated as a classical problem of laminar flow between plates, with transmissivity of the microannulus derived from the cubic law (Witherspoon et al., 1980). Under this assumption, transmissivity would increase with the cube of the aperture, pointing to the significance of the larger peak aperture observed in test B2. It can be concluded that the pre-existing defect resulted in the development of a microannulus with greater capacity for upward migration of CO_2.

8 | CONCLUSIONS

This study presented a coupled thermo-poroelastic model of a CO_2 injection well and a near-well region, with casing, cement, and formation interfaces described using cohesive interface elements and a traction–separation law. The coupled thermal, hydraulic, and mechanical behavior in the model was verified using an analytical solution, after which the model was applied to investigate interface damage initiation and development under pressure and cold thermal loading associated with CO_2 injection over a 30-day simulation period. Four simulations were performed with a consistent injection pressure of 20 MPa and an injection temperature of either 20 or 10°C. The first set of simulations considered intact wells without any pre-existing defects, while the second set of simulations introduced pre-existing debonding at the casing–cement interface.

Analysis of the thermo-poroelastic response of the well system established key differences in the evolution of temperature, stress, and displacement in the casing, cement, and formation. Changes in pore pressure were found to be less significant, since all simulations were performed for a 2D plane strain well section located above the injection interval in the cap rock, meaning that there was no mass transfer from the well tubing. Temperature was found to rapidly equilibrate in the casing due to its higher thermal conductivity and lower specific heat capacity, while the cement and rock temperature continued to evolve during the simulation period. Under the conditions considered, tensile radial stress developed at both the casing–cement and cement–formation interfaces, while hoop stress in the cement sheath remained in compression after 30 days, reducing the risk of radial cracking. However, the magnitude of compressive hoop stress reduced at the lower injection temperature, suggesting a greater risk of tensile stress and cracking as the temperature is reduced, which needs to be investigated under a wider range of conditions.

The main contribution of this study has been to bridge two types of studies already available in the literature: (1) staged numerical models that have stringently modeled various stages of well construction and operation without attention to defects and (2) utilization factor models that have been used to determine failure modes but cannot predict the extent and aperture of debonding. The investigation found that interface damage occurred at the casing–cement interface for simulations at the lower injection temperature. No such damage was predicted at the higher injection temperature, and no damage occurred at the cement–formation interface at either temperature. Pre-existing debonding (i.e., a defect) at the casing–cement interface led to slightly earlier damage initiation, after 2.75 days compared to 4 days, but critically, more than doubled the peak microannulus aperture from 0.037 to 0.077 mm, with the implication of significantly higher vertical transmissivity for CO_2 leakage. Of practical significance, under the conditions of the simulations considered, it may be concluded that the damage window for the casing–cement interface aligned with representative conditions for CO_2 injection. More generally, since damage to a well does not necessarily imply loss of integrity, leakage risk assessments should be informed by models that not only predict the onset of damage but also its development and the associated increase in upward CO_2 migration.

Having established and applied the model here, future work will remove key assumptions and encompass a broader investigation of greater practical significance to the engineering design of CO_2 injection wells. The priorities in this regard are as follows:

1. A sensitivity study for geometric and material parameters, initial and boundary conditions, and pre-existing defect type and extent. The focus should be on the interface properties (tensile and shear strength, energy release rates, etc.), including differences at the casing–cement and cement–formation interfaces, since various values are reported in the literature.
2. Periodic injection rather than the ramped and stable injection considered here, which would better represent operating conditions at a CO_2 storage site.
3. Moving from a 2D plane strain well section to a 3D well section to improve the translation of damage development into leakage risk.
4. Extension of the theoretical framework to account for crack initiation and propagation.
5. Extension of the theoretical framework and simulation domain to include the injection interval in addition to the cap rock, requiring the consideration of mass transfer from the well and multiphase flow as CO_2 displaces the formation water.

AUTHOR CONTRIBUTIONS

Lee J. Hosking: Conceptualization; formal analysis; funding acquisition; investigation; methodology; project administration; software; validation; visualization; writing—original draft preparation. **Xiangming Zhou**: Writing—review and editing.

ACKNOWLEDGMENTS

This study was performed as part of the C-WELL project supported by the UK Carbon Capture and Research Community (UKCCSRC) Flexible Funding Call 2023.

CONFLICT OF INTEREST STATEMENT

The authors declare no conflict of interest.

DATA AVAILABILITY STATEMENT

The data presented in this paper can be accessed from Brunel University London's data repository, Brunelfigshare, under a CCBY licence. A DOI link to the data will be provided and included here before publication.

ORCID

Lee J. Hosking http://orcid.org/0000-0002-5111-0416

REFERENCES

Ahmed S, Salehi S. Failure mechanisms of the wellbore mechanical barrier systems: implications for well integrity. *J Energy Resour Technol*. 2021;143(7):073007. doi:10.1115/1.4050694

de Andrade J, Sangesland S. Cement sheath failure mechanisms: numerical estimates to design for long-term well integrity. *J Petrol Sci Eng*. 2016;147:682-698. doi:10.1016/j.petrol.2016.08.032

de Andrade J, Sangesland S, Todorovic J, Vrålstad T. Cement sheath integrity during thermal cycling: a novel approach for experimental tests of cement systems. *SPE Bergen One Day Seminar, Bergen, Norway*, SPE-173871-MS. 2015. doi:10.2118/173871-MS

de Andrade J, Torsæter M, Todorovic J, Opedal N, Stroisz A, Vrålstad T. *Influence of casing centralization on cement sheath integrity during thermal cycling. IADC/SPE Drilling Conference and Exhibition, Fort Worth, Texas, USA*, SPE-168012-MS. 2014. doi:10.2118/168012-MS

Benzeggagh ML, Kenane M. Measurement of mixed-mode delamination fracture toughness of unidirectional glass/epoxy composites with mixed-mode bending apparatus. *Compos Sci Technol*. 1996;56(4):439-449. doi:10.1016/0266-3538(96)00005-X

Bishop AW. The influence of an undrained change in stress on the pore pressure in porous media of low compressibility. *Géotechnique*. 1973;23(3):435-442. doi:10.1680/geot.1973.23.3.435

Carroll S, Carey JW, Dzombak D, et al. Review: role of chemistry, mechanics, and transport on well integrity in CO_2 storage environments. *Int J Greenhouse Gas Control*. 2016;49:149-160. doi:10.1016/j.ijggc.2016.01.010

COMSOL. *Structural Mechanics Module User's Guide*. COMSOL; 2022.

Crow W, Carey JW, Gasda S, Brian Williams D, Celia M. Wellbore integrity analysis of a natural CO_2 producer. *Int J Greenhouse Gas Control*. 2010;4(2):186-197. doi:10.1016/j.ijggc.2009.10.010

Duguid A, Kirksey J, Riestenberg D, et al. CO_2 well construction: lessons learned from United States department of Energy Sponsored Projects. *14th Greenhouse Gas Cont Technol Conf*. 2018. doi:10.2139/ssrn.3365869

Goodwin KJ, Crook RJ. Cement sheath stress failure. *SPE Dril Eng*. 1992;7(4):291-296. doi:10.2118/20453-PA

Huan X, Xu G, Zhang Y, Sun F, Xue S. Study on thermo-hydro-mechanical coupling and the stability of a geothermal wellbore structure. *Energies*. 2021;14(3):649. doi:10.3390/en14030649

IPCC. Global warming of 1.5°C. An IPCC special report on the impacts of global warming of 1.5°C above pre-industrial levels and related global greenhouse gas emission pathways, in the context of strengthening the global response to the threat of climate change. *Int Panel Clim Change*. 2018;1-24. https://www.ipcc.ch/

Jackson PB, Murphey CE. *Effect of casing pressure on gas flow through a sheath of set cement. SPE/IADC Drilling Conference, Amsterdam, Netherlands*, SPE-25698-MS. 1993. doi:10.2118/25698-MS

Khalili N, Selvadurai APS. A fully coupled constitutive model for thermo-hydro-mechanical analysis in elastic media with double porosity. *Geophys Res Lett*. 2003;30(24). doi:10.1029/2003GL018838

King GE, King DE. Environmental risk arising from well-construction failure—differences between barrier and well failure, and estimates of failure frequency across common well types, locations, and well age. *SPE Produ Operat*. 2013;28(4):323-344. doi:10.2118/166142-PA

Kuanhai D, Yue Y, Yi H, Zhonghui L, Yuanhua L. Experimental study on the integrity of casing-cement sheath in shale gas wells under pressure and temperature cycle loading. *J Petrol Sci Eng*. 2020;195:107548. doi:10.1016/j.petrol.2020.107548

Lavrov A. Stiff cement, soft cement: nonlinearity, arching effect, hysteresis, and irreversibility in CO_2-well integrity and near-well geomechanics. *Int J Greenhouse Gas Control*. 2018;70:236-242. doi:10.1016/j.ijggc.2017.11.012

Li X-R, Gu C-W, Ding Z-C, Feng Y-C. THM coupled analysis of cement sheath integrity considering well loading history. *Petrol Sci*. 2023;20(1):447-459. doi:10.1016/j.petsci.2022.09.001

Li Z, Zhang K, Guo X, Liu J, Cheng X, Du J. Study of the failure mechanisms of a cement sheath based on an equivalent physical experiment. *J Nat Gas Sci Eng*. 2016;31:331-339. doi:10.1016/j.jngse.2016.03.037

Liu W, Yu B, Deng J. Analytical method for evaluating stress field in casing-cement-formation system of oil/gas wells. *Appl Math Mech*. 2017;38(9):1273-1294. doi:10.1007/s10483-017-2237-8

Liu Z, Deng Z, Davis SJ, Ciais P. Global carbon emissions in 2023. *Nat Rev Earth Eng*. 2024;5(4):253-254. doi:10.1038/s43017-024-00532-2

Najari M, Selvadurai APS. Thermo-hydro-mechanical response of granite to temperature changes. *Environ Earth Sci*. 2014;72(1):189-198. doi:10.1007/s12665-013-2945-3

Roberts JJ, Stalker L. What have we learnt about CO_2 leakage from CO_2 release field experiments, and what are the gaps for the future? *Earth-Sci Rev*. 2020;209:102939. doi:10.1016/j.earscirev.2019.102939

Roy P, Morris JP, Walsh SDC, Iyer J, Carroll S. Effect of thermal stress on wellbore integrity during CO_2 injection. *Int J Greenhouse Gas Control*. 2018;77:14-26. doi:10.1016/j.ijggc.2018.07.012

Selvadurai APS, Nguyen TS. Computational modelling of isothermal consolidation of fractured porous media. *Comp Geotech*. 1995;17(1):39-73. doi:10.1016/0266-352X(95)91302-K

Selvadurai APS, Suvorov AP. *Thermo-Poroelasticity and Geomechanics*. Cambridge University Press; 2016. doi:10.1017/CBO9781316543832

Stormont JC, Fernandez SG, Taha MR, Matteo EN. Gas flow through cement-casing microannuli under varying stress conditions. *Geomech Energy Environ*. 2018;13:1-13. doi:10.1016/j.gete.2017.12.001

Sule I, Imtiaz S, Khan F, Butt S. Nonlinear model predictive control of gas kick in a managed pressure drilling system. *J Petrol Sci Eng*. 2019;174:1223-1235. doi:10.1016/j.petrol.2018.11.046

Taghipour A, Ghaderi A, Cerasi P, Gheibi S. Novel laboratory setup for realistic wellbore cement and formation integrity studies. *J Petrol Sci Eng*. 2022;208:109664. doi:10.1016/j.petrol.2021.109664

Therond E, Bois A-P, Whaley K, Murillo R. Large-scale testing and modeling for cement zonal isolation in water-injection wells. *SPE Dril Comp*. 2017;32(4):290-300. doi:10.2118/181428-PA

Torsæter M, Todorovic J, Lavrov A, et al. Avoiding damage of CO_2 injection wells caused by temperature variations. *Energy Proc*. 2017;114:5275-5286. doi:10.1016/j.egypro.2017.03.1645

Valov AV, Golovin SV, Shcherbakov VV, Kuznetsov DS. Thermoporoelastic model for the cement sheath failure in a cased and cemented wellbore. *J Petrol Sci Eng*. 2022;210:109916. doi:10.1016/j.petrol.2021.109916

Vilarrasa V, Rutqvist J. Thermal effects on geologic carbon storage. *Earth Sci Rev*. 2017;165:245-256. doi:10.1016/j.earscirev.2016.12.011

Vilarrasa V, Silva O, Carrera J, Olivella S. Liquid CO_2 injection for geological storage in deep saline aquifers. *Int J Greenhouse Gas Control*. 2013;14:84-96. doi:10.1016/j.ijggc.2013.01.015

Viswanathan HS, Pawar RJ, Stauffer PH, et al. Development of a hybrid process and system model for the assessment of wellbore leakage at a geologic CO_2 sequestration site. *Environ Sci Technol*. 2008;42(19):7280-7286. doi:10.1021/es800417x

Witherspoon PA, Wang JSY, Iwai K, Gale JE. Validity of cubic law for fluid flow in a deformable rock fracture. *Water Resour Res*. 1980;16(6):1016-1024. doi:10.1029/WR016i006p01016

Zhang M, Bachu S. Review of integrity of existing wells in relation to CO_2 geological storage: what do we know? *Int J Greenhouse Gas Control*. 2011;5(4):826-840. doi:10.1016/j.ijggc.2010.11.006

Zhang W, Eckert A. Micro-annulus generation under downhole conditions: insights from three-dimensional staged finite element analysis of cement hardening and wellbore operations. *J Rock Mech Geotech Eng*. 2020;12(6):1185-1200. doi:10.1016/j.jrmge.2020.03.003

Zhang W, Eckert A, Liu X. Numerical simulation of micro-annuli generation by thermal cycling. *51st U.S. Rock Mech Geomech Symp. ARMA-2017-0354*. 2017.

APPENDIX A

This appendix contains the set of analytical solutions for one-dimensional problems of thermo-poroelasticity presented by Selvadurai and Suvorov (2016) and shown in Figure 4. The initial and boundary conditions are summarized as follows:

$$u_x(L,t) = 0, \tag{A1}$$

$$\sigma_{xz}(0,t) = \sigma_{xy}(0,t) = 0, \tag{A2}$$

$$\sigma_{xx}(0,t) = \sigma_0, \tag{A3}$$

$$p(0,t) = 0, \tag{A4}$$

$$\left(\frac{k}{\mu}\frac{\partial p}{\partial x}\right)_{x=L} = 0, \tag{A5}$$

$$\left(\lambda^* \frac{\partial T}{\partial x}\right)_{x=L} = 0, \tag{A6}$$

$$T(0,t) = \overline{T}_0, \tag{A7}$$

where λ^* is the overall thermal conductivity of the poroelastic material, noting that C^* in Table 1 is similarly the overall gravimetric specific heat, σ_0 and $\overline{T}_0$ are the prescribed constant normal stress and temperature at the upper boundary, respectively, and Equation (A4) defines the drained upper boundary condition of the poroelastic material.

The solutions for temperature, pore pressure, and displacement are now presented in their final form, Selvadurai and Suvorov (2016):

$$T(x,t) = T_0 \sum_{m=1,3,5,\ldots} \frac{4}{m\pi} \sin\left(\frac{m\pi}{2L}x\right) \exp\left(-\kappa_m^2 t\right), \tag{A8}$$

$$\begin{aligned} p(x,t) = p_0 &\sum_{m=1,3,5,\ldots} \frac{4}{m\pi} \sin\left(\frac{m\pi}{2L}x\right) \exp\left(-\omega_m^2 t\right) \\ &- \sum_{m=1,3,5,\ldots} A_m \frac{4}{m\pi} \sin\left(\frac{m\pi}{2L}x\right) \exp\left(-\omega_m^2 t\right) \\ &+ \sum_{m=1,3,5,\ldots} A_m \frac{4}{m\pi} \sin\left(\frac{m\pi}{2L}x\right) \exp\left(-\kappa_m^2 t\right), \end{aligned} \tag{A9}$$

$$\begin{aligned} u(x,t) = \frac{1}{K_D + 4G_D/3} \times \Big[&-\textstyle\sum_{m=1,3,5,\ldots} (K_D 3\alpha_s T_0 + \alpha_B A_m) \\ &\frac{8L}{m^2\pi^2} \cos\left(\frac{m\pi}{2L}x\right) \exp\left(-\kappa_m^2 t\right) \\ &+ \textstyle\sum_{m=1,3,5,\ldots} \alpha_B (A_m - p_0) \frac{8L}{m^2\pi^2} \cos\left(\frac{m\pi}{2L}x\right) \\ &\exp\left(-\omega_m^2 t\right) + \sigma_0 (x - L) \quad \Big], \end{aligned} \tag{A10}$$

where

$$\kappa_m^2 = \frac{m^2\pi^2}{4L^2} \frac{\lambda^*}{C^*}, \tag{A11}$$

$$\omega_m^2 = \frac{k}{\mu} \frac{m^2\pi^2}{4L^2} \frac{K_\mathrm{D} + \frac{4G_\mathrm{D}}{3}}{\left(\frac{\phi}{\mathrm{K_f}} + \frac{\alpha_\mathrm{B} - \phi}{K_\mathrm{s}}\right)\left(K_\mathrm{D} + \frac{4G_\mathrm{D}}{3}\right) + \alpha_\mathrm{B}^2}, \tag{A12}$$

$$A_m = -T_0 \frac{\phi 3\alpha_\mathrm{f} + (\alpha_\mathrm{B} - \phi) 3\alpha_\mathrm{s} - \frac{\alpha_\mathrm{B} K_\mathrm{D}}{K_\mathrm{D} + 4G_\mathrm{D}/3} 3\alpha_\mathrm{s}}{\frac{k}{\mu}\frac{C^*}{\lambda^*} - \left(\frac{\phi}{K_\mathrm{f}} + \frac{\alpha_\mathrm{B} - \phi}{K_\mathrm{s}} + \frac{\alpha_\mathrm{B}^2}{K_\mathrm{D} + 4G_\mathrm{D}/3}\right)}, \tag{A13}$$

where G_D is the undrained shear modulus. All equations and terms are fully developed by Selvadurai and Suvorov (2016).

AUTHOR BIOGRAPHY

Dr. Lee J. Hosking is a senior lecturer in Energy Geomechanics at Brunel University of London (Department of Civil and Environmental Engineering). His research focuses on theoretical and numerical modeling of deep subsurface environments, with a focus on coupled thermal–hydraulic–mechanical (THM) phenomena, accurate and efficient fracture network representation, and damage evolution via debonding and cracking. For over 10 years, the main practical application of his research has been geological CO_2 storage with respect to storage capacity, injectivity, and migration/confinement. He has also investigated the potential of unconventional geothermal energy systems in Great Britain.

How to cite this article: Hosking LJ, Zhou X. Damage modeling of CO_2 injection well interfaces under coupled thermal, hydraulic and mechanical behavior. *Deep Undergr Sci Eng*. 2025;4(4): 762-776. doi:10.1002/dug2.70014